Stability of Supersonic Boundary Layers Over Blunt Wedges

P.Balakumar*
NASA Langley Research Center, Hampton, VA 23681

Receptivity and stability of supersonic boundary layers over blunt flat plates and wedges are numerically investigated at a free stream Mach number of 3.5 and at a high Reynolds number of 10^6/inch. Both the steady and unsteady solutions are obtained by solving the full Navier-Stokes equations using the 5^{th}-order accurate weighted essentially non-oscillatory (WENO) scheme for space discretization and using third-order total-variation-diminishing (TVD) Runge-Kutta scheme for time integration. Computations are performed for a flat plate with leading edge thicknesses of 0.0001, 0.001, 0.005 and 0.01 inches that give Reynolds numbers based on the leading edge thickness ranging from 1000 to 10000. Calculations are also performed for a wedge of 10 degrees half angle with different leading edge radii 0.001 and 0.01 inches. The linear stability results showed that the bluntness has a strong stabilizing effect on the stability of two-dimensional boundary layers. The transition Reynolds number for a flat plate with a leading edge thickness of 0.01 inches is about 3.5 times larger than it is for the Blasius boundary layer. It was also revealed that boundary layers on blunt wedges are far more stable than on blunt flat plates.

Introduction

Transition from laminar to turbulent state in shear flows occurs due to evolution and interaction of different disturbances inside the shear layer. Though there are several mechanisms and routes to go from a laminar to a turbulent state, most of them generally follow these fundamental processes:

- Receptivity
- Linear instability
- Nonlinear instability and saturation
- Secondary instability and breakdown to turbulence

In the receptivity process, unsteady disturbances in the environment such as acoustic waves and turbulence interact with the inhomogeneities in the geometry such as roughness and generate instability waves inside the shear layer. In quiet environments, the initial amplitudes of these instability waves are small compared to any characteristic velocity and length scales in the flow. In the linear instability stage, the amplitudes of these instability waves grow exponentially downstream and this process is governed by the linearized Navier-Stokes equations. Further downstream, the amplitudes of the disturbances become large and the nonlinear effects inhibit the exponential growth and the amplitude of the waves eventually saturate. In the next stage, these finite amplitude saturated disturbances become unstable to two- and/or three-dimensional disturbances. This is called the secondary instability and beyond this stage the spectrum broadens, due to complex interactions and further instabilities, and the flow becomes turbulent in a short distance downstream. In previous studies[1,2], the interactions of two and three-dimensional

---

* Aerospace Engineer, Flow Physics and Control Branch, NASA Langley Research Center, MS 170, AIAA Member.

acoustic disturbances with and without isolated two-dimensional roughness elements in a supersonic boundary layer were investigated. The simulations showed that the linear instability waves are generated very close to the leading edge. The wavelength of the disturbances inside the boundary layer first increases gradually and becomes longer than the wavelength for the instability waves within a short distance from the leading edge. The wavelength then decreases gradually and merges with the wavelength for the Tollmien_Schlichting wave. The initial amplitudes of the instability waves near the neutral points, the receptivity coefficients, are about 1.20 and 0.07 times the amplitude of the free-stream disturbances for the slow and the fast waves respectively. It was also revealed that a small isolated roughness element does not enhance the receptivity process for the given nose bluntness. In this paper, the stability and generation of instability waves by acoustic disturbances in supersonic boundary layers over blunt flat plates and wedges with a free stream Mach number of 3.5 are investigated.

The transition process mainly depends on the boundary layer characteristics and on the frequency, wave number distributions, and the amplitudes of the disturbances that enter the boundary layer. The boundary layer profiles depend on the flow parameters such as Mach number, Reynolds number, wall temperature, and model geometry. In supersonic and hypersonic boundary layers one important geometrical parameter is the leading edge bluntness. The effects of bluntness on transition have been studied experimentally and numerically by many researchers[3-8]. It was found that the bluntness generally stabilizes the boundary layer. The critical Reynolds numbers for blunt cones are much higher compared to that for sharp cones. However, the transition Reynolds number increased only by a factor of two compared to the sharp cones. It was identified that the entropy layer that is formed near the bow shock region persists for a long distance downstream and makes the boundary layer more stable compared to the sharp cone case. After the entropy layer and the boundary layer that is developing along the surface merges together, the boundary layer becomes unstable. It was also found that in addition to first and the second modes instability waves, other inviscid type disturbances grow inside the entropy layer. It is also observed that with increasing bluntness the stabilizing trend is reversed in axi-symmetric boundary layers. Another influence of the bluntness is in the generation of instability waves near the leading edge region. The objectives of this work are to estimate the stabilizing effect of the bluntness on the supersonic boundary layers over blunt flat plates and wedges and to estimate the receptivity coefficient of the instability waves generated near the leading edge. To investigate the effect of the Reynolds number based on the nose bluntness, simulations are performed at different leading edge thickness b = 0.0001, 0.001, 0.005 and 0.01 inches and at a unit Reynolds number of $1.0*10^6$/inch for a flat plate and at nose radii of r_0 = 0.001 and 0.01 for a 10 degrees wedge. One simulation is also performed at a higher unit Reynolds number of $4.0*10^6$/inch with 0.01 inches bluntness. This causes the Reynolds number based on the nose radius to vary from 10^2 to $4*10^4$. The results consist of: (1) mean flow profiles, linear stability and transition onset Reynolds numbers for flat plates and wedges at different bluntness, and (2) receptivity coefficients for different bluntness. A schematic diagram of the computational set up is depicted in Fig. 1.

Governing Equations.

The equations solved are the three-dimensional unsteady compressible Navier-Stokes equations in conservation form

$$\frac{\partial}{\partial t} Q_i + \frac{\partial}{\partial x_j} \left(F_{ji} - F_{vji} \right) = 0. \qquad (1)$$

$$\text{Here } Q_i = \begin{Bmatrix} \rho \\ \rho E \\ \rho u \\ \rho v \\ \rho w \end{Bmatrix} \quad [F_{ji}] = \begin{Bmatrix} \rho u_j \\ (\rho E + p)u_j \\ \rho u u_j + \delta_{1j} p \\ \rho v u_j + \delta_{2j} p \\ \rho w u_j + \delta_{3j} p \end{Bmatrix} \quad [F_{vij}] = \begin{Bmatrix} 0 \\ u\tau_{1j} + v\tau_{2j} + w\tau_{3j} - q_j \\ \tau_{1j} \\ \tau_{2j} \\ \tau_{3j} \end{Bmatrix}. \tag{2}$$

Here *(x, y, z)* are the Cartesian coordinates, (*u, v ,w*) are the velocity components, ρ is the density, and *p* is the pressure. *E* is the total energy given by

$$E = e + \frac{u^2 + v^2 + w^2}{2},$$

$$e = c_v T, \; p = \rho RT. \tag{3}$$

Here *e* is the internal energy and *T* is the temperature. The shear stress and the heat flux are given by

$$\tau_{ij} = \mu\left\{\frac{\partial u_i}{\partial x_j} + \frac{\partial u_j}{\partial x_i} - \frac{2}{3}\delta_{ij}\frac{\partial u_k}{\partial x_k}\right\}, \quad q_j = -k\frac{\partial T}{\partial x_j}. \tag{4}$$

The viscosity (μ) is computed using Sutherland's law and the coefficient of conductivity (*k*) is given in terms of the Prandtl number *Pr*. The variables ρ, *p, T* and velocity are non-dimensionalised by their corresponding reference variables ρ_∞, p_∞, T_∞ and $\sqrt{RT_\infty}$ respectively. The reference value for length is computed by $\sqrt{\nu x_0 / U_\infty}$, where x_0 is a reference location. For the computation, the equations are transformed from physical coordinate system (*x, y, z*) to the computational curvilinear coordinate system (ξ, η, ζ) in a conservative manner and the governing equations become

$$\frac{\partial}{\partial t}\overline{Q}_i + \frac{\partial}{\partial x_j}\left(\overline{F}_{ji} - \overline{F}_{vji}\right) = 0. \tag{5}$$

The components of the flux in the computational domain are related to the flux in the Cartesian domain by

$$\overline{Q}_i = \frac{Q_i}{J}, \quad [\overline{F}_{ji}] = \frac{J}{|J|}[F_{ji}] \tag{6}$$

where $J = \left[\dfrac{\partial(\xi, \eta, \zeta)}{\partial(x, y, z)}\right]$.

Solution Algorithm

The governing equations are solved using a 5th order accurate WENO scheme for space discretization and using a third order, total variation diminishing (TVD) Runge-Kutta scheme for time integration. These methods are suitable in flows with discontinuities or high gradient regions. These schemes solve the governing equations discretely in a uniform structured computational domain in which flow properties are known point wise at the grid nodes. They approximate the spatial derivatives in a given direction to a higher order at the nodes, using the neighboring nodal values in that direction, and they integrate the resulting equations in time to get the point values as a function of time. Since the spatial derivatives are independent of the coordinate directions, the method can easily add multidimensions. It is well known that approximating a discontinuous function by a higher order (two or more) polynomial generally

introduces oscillatory behavior near the discontinuity, and this oscillation increases with the order of the approximation. The essentially nonoscillatory (ENO) and the improvement of these WENO methods are developed to keep the higher order approximations in the smooth regions and to eliminate or suppress the oscillatory behavior near the discontinuities. They are achieved by systematically adopting or selecting the stencils based on the smoothness of the function, which is being approximated. Ref.9 explains the WENO and the TVD methods and the formulas and Ref.10 gives the application of the ENO method to the N-S equations. Ref.11 describes in detail the solution method implemented in this computation.

At the outflow boundary, characteristic boundary conditions are used. At the wall, the simulation uses viscous conditions for the velocities and a constant temperature condition, and it computes density from the continuity equation. This wall temperature is approximately equivalent to adiabatic wall condition. In the spanwise direction, symmetric and periodic conditions are used at the boundaries. In the mean flow computations, the simulation prescribes the free-stream values at the upper boundary, which lies outside the bow shock. In the unsteady computations, it superimposes the acoustic perturbations to the uniform mean flow at the upper boundary. The procedure is to first compute the steady mean flow by performing unsteady computations using a variable time step until the maximum residual reaches a small value ~10^{-11}. These computations use a CFL number of 0.4. The next step is to introduce unsteady disturbances at the upper boundary of the computational domain and to perform time accurate computations to investigate the interaction and evolution of these disturbances downstream.

The grid is generated using analytical formulae. The grid stretches in the η direction close to the wall and is uniform outside the boundary layer. In the ξ direction, the grid is symmetric about the leading edge and very fine near the nose and is uniform in the flat region. The grid is uniform in the spanwise direction. The outer boundary that lays outside of the shock follows a circle near the nose region with its vertex located a short distance upstream of the nose and follows a parabola downstream of the nose to capture the boundary layer accurately. The computational domain extends from x = -0.015 to 72.0 inches in the axial direction depending on the transition Reynolds numbers. Calculations were performed using different grid sizes varying from (2001*251*11) to (4001*301*11) depending on the size of the domain. Due to the very fine grid requirement near the nose, the allowable time step is very small and the computations become very expensive to simulate the unsteady computations in the entire domain at once. To overcome this, calculations are performed in two steps. First, the computations are done near the nose region with a very small time step. Second, the flow properties in the middle of this domain are fed as inflow conditions for the second larger domain and the computations are carried out with a larger time step.

The symmetric acoustic field that impinges on the outer boundary is taken to be in the following form.

$$\begin{aligned} p'_{ac} &= \mathrm{Real}\left\{\tilde{p}_{ac} e^{i\alpha_{ac}x \pm i\beta z + i\varepsilon_{ac}y - i\omega t}\right\} \\ &\quad + \mathrm{Real}\left\{\tilde{p}_{ac} e^{i\alpha_{ac}x \pm i\beta z - i\varepsilon_{ac}y - i\omega t}\right\}. \end{aligned} \tag{7}$$

Here α_{ac}, β_{ac}, ε_{ac} are the acoustic wavenumber, and ω is the frequency of the acoustic disturbance. The wavenumber in the y-direction ε_{ac} determines the incident angle of the acoustic waves and in this paper computations are performed for zero incident angle, ε_{ac} = 0.

Results

Computations are performed for supersonic flows over semi-infinite flat plates and wedges with blunt leading edges. Table 1 gives the flow parameters and Fig. 1 shows the schematic diagram of the computational set up. The leading edge of the flat plate is modeled as a super ellipse of the form

$$\frac{(x-a)^4}{a^4}+\frac{y^2}{b^2}=1. \tag{8}$$

Here b is the half thickness of the plate and computations are performed for several values of thickness b = 0.0001, 0.001, 0.005, 0.01 inches. It should be noted that sharp flat-plate experiments, in general, employ beveled leading edges with very small leading edge radii. In the computations, the beveled edges are modeled as thin flat plates with small bluntness. The aspect ratio a/b is taken as 10 hence the blunt leading edge is joined with the straight portion of the plate at $x = 10b$. For a free stream unit Reynolds number of $1.0*10^6$/inch, these leading edge thicknesses give the Reynolds numbers based on the leading edge thickness Re_b equal to 10^2, 10^3, $5*10^3$ and 10^4.

Simulations are also performed for M = 3.5 over a wedge with 10 degrees half angle. The conditions behind the oblique shocks for different wedge angles are given in Table 2. The nose region of the wedge is modeled as a circle of the form

$$(x-r_0)^2+y^2=r_0^2. \tag{8}$$

Here r_0 is the radius of the leading edge bluntness. Simulations are performed for nose radii r_0 = 0.001 and 0.01 inches at a unit Reynolds numbers $1.0*10^6$/inch. This provides nose Reynolds numbers of 10^3, 10^4. To achieve a higher nose Reynolds number of $4*10^4$, one computation is performed at a unit Reynolds number of $4.0*10^6$/inch with a nose radius of r_0 = 0.01 inches. Different cases are summarized in Table 3.

Table 1 Flow parameters used in the computation.

Free stream Mach number: M_∞=3.5

Free stream Reynolds number: Re_∞=$1.0*10^6$/in.

Free stream density: ρ_∞=$2.249*10^{-2}$ lbm/ft^3

Free stream pressure: p_∞=187.74 lbf/ft^2

Free stream velocity: U_∞=2145.89 ft/s

Free stream temperature: T_∞=156.42 $^\circ$R

Free stream kinematic viscosity: ν_∞ =$1.7882*10^{-4}$ ft^2/s

Wall temperature: T_w=476 $^\circ$R

Prandtl number: Pr= 0.72

Ratio of specific heats: γ=1.4

Length scale $\sqrt{\frac{\nu_\infty x_0}{U_\infty}} = 5.892*10^{-5}$ *ft.* ($x_0 = 0.5$ in.)

The boundary layer thickness at x=1 in.: δ_0= .01275 in.

Non–dimensional frequency F=$1*10^{-5}$ is equivalent to 41.0 kHz

The non-dimensional frequency F is defined as $F=\frac{2\pi\nu_\infty f}{U_\infty^2}$,

where *f* is the frequency in Hertz.

Table 2 Conditions downstream of the shock.

Wedge angle, deg.	Shock angle, deg.	Mach number	Pressure ratio	Density ratio	Temperature ratio	Unit Reynolds number ratio
10	24.384	2.904	2.269	1.767	1.284	1.28
20	34.602	2.298	4.442	2.648	1.677	1.34
30	47.755	1.655	7.665	3.438	2.229	1.12

Table 3 Parameters in the computations.

Nose radius r_0 in.	Unit Reynolds number /in.	Reynolds number based on nose radius
0.0001	$1.0*10^6$	10^2
0.001	$1.0*10^6$	10^3
0.005	$1.0*10^6$	$5*10^3$
0.01	$1.0*10^6$	10^4
0.01	$4.0*10^6$	$4*10^4$

Linear instability

The linear stability results for the similarity boundary layer over the wedge at conditions downstream of the shock are presented in Fig. 2. The stability diagram for a flat plate is given in Ref. 1. The figure depicts the neutral stability diagram in the (*Re, F*) plane for different wave angles 0, 45 and 60 degrees. The figure also shows the N-Factor curves and the growth rates for the most amplified disturbances. Here, the variables are non-dimensionalized by the variables downstream of the shock. To obtain the variables non-dimensionalized by the free stream values as given in Table 1, the variables in this section should be multiplied by the appropriate factors. The frequency variable F has to be multiplied by 1.2 to obtain in terms of free stream values. The critical Reynolds number is about 209 and this occurs for an oblique wave of angle 60 degrees. The most amplified frequencies are in the range $F = 0.075\text{-}1.25*10^{-5}$ and the spanwise wave number of the most amplified wave is about $\beta = 0.025$. This corresponds to 0.178 inches in dimensional units and is equivalent to about 14 boundary layer thicknesses. It is also observed that at higher Reynolds numbers $Re > 1000$, only the low frequency disturbances $F < 3.0*10^{-5}$ are unstable. This implies that an acoustic disturbance with frequencies less than 120 kHz may be the relevant frequency

range for generating instability waves inside the boundary layer. The frequency of the most amplified wave is about 40-50 kHz and the maximum N-factor at x = 12 in. (Re = 3464) is about 8.6.

Mean flow and linear stability for the flat plate

Figure 3 shows the mean flow density contours extracted from the Navier-Stokes computations. Figure 3(a) shows the entire domain for the leading edge bluntness of b = 0.01 in. and Figs. 3 (b), (c), (d) show the flow field near the leading edge for the leading edge bluntness b = *0.01, 0.001, 0.0001* inches. The leading edge shocks are located approximately at $7.7*10^{-4}$, $6.0*10^{-6}$, and $4.0*10^{-7}$ in. upstream of the leading edge. Figure 4 shows the Mach number distributions along the boundary layer edge for the three different bluntness cases. The Mach number distributions reach constant values within a short distance from the leading edge. The density profiles at different axial locations are plotted in Figs. 5(a)-(c) for the different bluntness cases b =*0.0001, 0.001* and *0.01* inches in the similarity coordinates. The compressible Blasius similarity profile is also included for comparison and Fig. 5(d) shows the profiles for b = *0.01* inches in the physical coordinate. It is seen that very close to the leading edge, there exists a strong shock and that the associated compression is followed by an expansion over the leading edge and the shock becomes weaker away from the leading-edge region. The boundary layer profiles with b = 0.0001 inches slowly approach the Blasius similarity profile close to x = 3 inches. With increasing bluntness, the profiles did not approach the similarity profiles within the computational domain, which is closer to the transition onset point. The difference between the profiles with the bluntness and the similarity profiles increases with the bluntness.

Figure 6 shows the growth rate and the N-Factors for the most amplified disturbances computed using the profiles obtained from the numerical simulation for different bluntness b = 0.0001, 0.001, 0.005, 0.01 inches. For comparison, the results for the Blasius similarity profiles, which model a sharp leading edge, are also shown in the figure. It is seen that the stability results and the N-Factor results obtained using the Navier-Stokes mean flow with the smallest bluntness b = 0.0001 agree reasonably well with those obtained using the Blasius similarity profiles. The frequency and the spanwise wave number for the most amplified wave are about $F = 1.25*10^{-5}$ and $\beta = 0.025$ in both cases. However, for larger bluntness, there is a significant difference both for the mean flow and the stability results as the growth rate becomes smaller and the N-Factor curve moves downstream. For the smaller bluntness b = 0.001, the N-Factor curve remains closer to the similarity curve. For the larger bluntness cases b = 0.005 and b = 0.01 the growth rates become smaller and the N-Factor curves move further to the right. The most amplified frequency and the spanwise wave number are ($0.80*10^{-5}$, 0.02), ($0.325*10^{-5}$, 0.01) ($0.325*10^{-5}$, 0.01) for b = 0.001, 0.005 and 0.01 inches respectively. This shows that the frequencies and the spanwise wave numbers of the most amplified disturbances become smaller with increasing bluntness. The growth rate curves are similar to the Blasius profile for smaller bluntness b = 0.0001 and 0.001 and at higher bluntness b = 0.005 and 0.01 they take a different shape. The growth rates first increase and plateau for a long distance and cause the disturbances to grow. For comparison, the growth rate and the N-Factor curve for $F = 0.30*10^{-5}$ and $\beta = 0.01$ for the similarity profiles are also shown in the figure. This has a larger growth rate than that for the bluntness case, however they have the same growth rate plateau at larger axial distances. It may be that at larger distances the boundary layer profiles have the similar stability characteristics as for the similarity profiles.

Boundary-layer transition data on a flat plate and on a cone, and free stream noise levels and the power spectral distribution of the free stream noise are presented in Ref. 12. The data shows the transition Reynolds number for a flat plate in quiet conditions is about $11*10^6$. If this is used in the correlation to obtain the N-Factor at the transition, the Fig. 6 gives an N-factor of 8.0 for a constant spanwise wave number. The transition Reynolds number obtained using this N-factor for different bluntness cases are summarized in Table 4 and is plotted in Fig. 7. The ratio between the transition Reynolds number with bluntness and the transition Reynolds number for the similarity profile, $(Re_T)_b/(Re_T)_{Similarity,}$ is about 1.05,

1.30, 2.48, 3.49 respectively for $Re_b = 10^2, 10^3, 5*10^3, 10^4$. In the experiment[12], when the thickness of the beveled leading edge was increased from 0.0001 inches to 0.001 inches, the transition Reynolds number increased from $11*10^6$ to $14.0*10^6$. This is an increase by a factor of 127. In the computations, when the half thickness of the flat plate was increased from 0.0001 inches to 0.001 inches the transition Reynolds number increased by a factor of 1.20. Even though the beveled edges are modeled as a thin flat plate in the computations, the computational results agree very well with the experimental results.

Table 4 Transition Reynolds number for the blunt flat plates.

Leading edge thickness b in.	Reynolds number based on b	Transition location X (in.)	Transition Reynolds number $*10^6$	Ratio $(Re_T)_b/(Re_T)_{Similarity}$
0.0	0	11.00	11.00	1.00
0.0001	10^2	11.77	11.77	1.05
0.001	10^3	14.12	14.12	1.30
0.005	$5*10^3$	27.30	27.30	2.48
0.01	10^4	38.37	38.37	3.49

Mean flow and Stability for the Wedge

Figure 8 shows the mean flow density contours computed using the WENO code. The figures 8(a-c) show the results for the wedge angle of 10 degrees at different nose radii r_0 = 0.001 and 0.01 inches. Smaller nose radii cases r_0 = 0.001 and 0.01 are performed at a unit Reynolds number of $1.0*10^6$/inch which yield Reynolds numbers based on the nose radius of 10^3 and 10^4. Figure 8(d) show the results obtained at a higher unit Reynolds number of $4.0*10^6$/inch with r_0 = 0.01 which yields the Reynolds number based on the nose radius of $4.0*10^4$. Figure 8(a) shows the density contours in larger domain and other figures show the flow field near the nose region. One interesting observation is that the inviscid density contours and the shock locations are same between Figs. 8(b) and (d) which are obtained with the same bluntness b = 0.01 but at different unit Reynolds numbers 1.0 and $4.0*10^6$. The leading edge shocks are located approximately at 0.0008 and 0.005 in. upstream of the leading edge. Figure 9 shows the Mach number distributions along the boundary layer edge for the different bluntness cases. The inviscid Mach number obtained from the shock conditions is also shown in the figure. The Mach number distributions reach constant values within a short distance from the leading edge. This suggests that the edge conditions are not the cause for the stabilization of the boundary layers in the cases with small bluntness. The density profiles at different axial locations are plotted in Fig. 10(a)-(c) for the different bluntness cases r_0 *=0.0001, 0.01, 0.01(Re/in. =4*10^6)* inches in the similarity coordinates. The compressible Blasius similarity profile is also included for comparison and Fig. 10(d) shows the profiles for r_0 = *0.01* inches in the physical coordinate. With increasing bluntness, the profiles did not approach the similarity profiles within the computational domain, which is closer to the transition onset point. The difference between the profiles with the bluntness and the similarity profiles increases with the bluntness.

Figure 11 shows the growth rate and the N-Factors for the most amplified disturbances computed using the profiles obtained from the numerical simulation for different bluntness r_0 = 0.001, 0.01, 0.01 (Re/in. = $4*10^6$) inches. For comparison, the results for the Blasius similarity profiles, which model a sharp leading edge, are also shown in the figure. The frequency and the spanwise wave number for the

most amplified wave are about F = 0.90*10^{-5} and β = 0.025 for the similarity profiles. However, for larger bluntness, there is significant difference both for the mean flow and the stability results when the growth rate becomes smaller and the N-Factor curve moves downstream. Foe the smaller bluntness r_0 = 0.001, the N-Factor curve remains closer to the similarity curve. For the larger bluntness cases r_0 = 0.01 and r_0 = 0.01 (4 mil) the growth rates become smaller and the N-Factor curves move further to the right. The most amplified frequency and the spanwise wave number are (0.60*10^{-5}, 0.02), (0.082*10^{-5}, 0.005) (0.175*10^{-5}, 0.0125) for r_0 = 0.001, 0.01 and 0.01 (4 mil) inches respectively. This shows that the frequencies of the most amplified disturbances become smaller with increasing bluntness. The growth rate curves are similar to the Blasius profile for smaller bluntness r_0 = 0.001 at higher bluntness r_0 = 0.01 and 0.01 (Re/in. = Re/inch = 4*10^{6}4 mil) they take a different shape as observed in the flat plate case. The growth rates first increase and plateau for a long distance and causes the disturbances to grow. The transition Reynolds numbers obtained using the N-factor of 8.0 for different bluntness cases are summarized in Table 5 and plotted in Fig. 7. The ratio between the transition Reynolds number with bluntness and the transition Reynolds number for the similarity profile, $(Re_T)_b/(Re_T)_{Similarity,}$ is about 1.42, 7.01, 11.96 respectively for Re_b = 10^3, 10^4, 4*10^4. Previous experiments[3] and the stability calculations[5] showed that the transition Reynolds number for a blunt cone at a Mach number of 8 with nose Reynolds numbers of 30,000 increased by a factor of 1.7~2.0 compared to a sharp cone. This implies that the bluntness effects are much stronger in flows over wedges than in flows over cones.

Table 5 Transition Reynolds number for the blunt wedges.

Nose radius r_0 in.	Reynolds number based on nose radius	Transition location X (in.)	Transition Reynolds number *10^6	Ratio $(Re_T)_b/(Re_T)_{Similarity}$
0.0	0	10.40	10.40	1.00
0.001	10^3	14.38	14.38	1.42
0.01	10^4	73.00	73.00	7.02
0.01 (4 mil)	4*10^4	28.50	114.0	10.96

Interaction of three-dimensional acoustic waves with the flat plate and wedge boundary layers.

After the mean flow is obtained, three-dimensional slow and fast acoustic disturbances are separately introduced at the outer boundaries and time accurate simulations are performed. The non-dimensional frequency and the spanwise wave number are F=1.25*10^{-5} and β = 0.025. These parameters give the largest N-factor close to the experimental transition location. To remain in the linear regime, very small initial amplitude of $\tilde{p}_{ac}/p_\infty = 1.0*10^{-7}$ is prescribed for the free-stream acoustic waves. Even with these small initial amplitudes, nonlinearity starts to develop near the end of the computational domain x ~ 10.0 inches. Details about the acoustic disturbances and the analysis to compute the wave numbers of the instability waves generated inside the boundary layer are described in Ref. 1.

Figure 12 shows the results for the evolution of the unsteady fluctuations obtained from the simulation for the slow wave at a fixed time for the case b = 0.0001 inches. Figure 12(a) shows the contours of the density fluctuations in the entire domain and Fig. 12(b) depicts the results inside the boundary layer. The perturbation field can be divided into four regions. One region is the area outside the shock where the acoustic waves propagate uniformly. The second region is the shock layer across which the acoustic waves are transmitted. The third region is the area between the shock and the boundary layer.

This region consists of transmitted external acoustic field and the disturbances that are radiated from the boundary layer. The fourth region is the boundary layer where the boundary layer disturbances evolve.

Figure 13 shows the amplitude of the pressure fluctuations along the wall in a log scale. Figure 13 also includes the results from the parabolized stability equations (PSE) computations obtained for the same mean boundary layer profiles. The figures clearly show the initial generation and the eventual exponential growth of the instability waves inside the boundary layer. The slow wave whose wavelength is closer to the wavelength of the instability wave transforms into instability waves smoothly. The fast waves whose wavelengths are much larger are initially modulated by short wavelength disturbances. These short waves transform into instability waves and grow exponentially downstream. The growth of the disturbances agrees very well with the PSE results about one acoustic wavelength downstream of the neutral point. Following the PSE results up to the neutral point, the initial amplitude of the instability waves at the neutral point can be estimated. From these values the receptivity coefficients defined by the initial amplitude of the pressure fluctuations at the wall at the neutral point non-dimensionalised by the free-stream acoustic pressure can be evaluated.

$$C_{recpt,p_{wall}} = \frac{(p_{wall})_n}{p_{ac}} \tag{15}$$

The computed receptivity coefficients for the slow and the fast waves are

$$\begin{aligned} C_{recpt,p_{wall},S} &= 1.20 \\ C_{recpt,p_{wall},F} &= 0.07 \end{aligned} \tag{16}$$

Similarly, the receptivity coefficients based on the maximum density fluctuations inside the boundary layer normalized by ρ_{ac} are calculated.

$$\begin{aligned} C_{recpt,\rho_{\max},S} &= 8.40 \\ C_{recpt,\rho_{\max},F} &= 0.47 \end{aligned} \tag{17}$$

The ratio of the receptivity coefficient between the slow and the fast modes are about 17.0. As expected, the slow modes, whose phase speeds are close to the neutral stability waves of the boundary layer, excite the instability waves more efficiently than the fast waves. Figure 14 shows the evolution of wall pressure fluctuations induced by the slow acoustic wave for larger bluntness cases b = 0.001 and b = 0.01 inches and the non-dimensional frequencies for these cases are F=1.25*10^{-5} and 0.75*10^{-5} respectively. The computed receptivity coefficients for the bluntness b = 0.001 and 0.01 are

$$\begin{aligned} C_{recpt,p_{wall},S} &= 1.18 \\ C_{recpt,p_{wall},S} &= 0.33 \end{aligned}$$

This shows that for smaller bluntness the receptivity coefficients are almost the same and for the larger bluntness case the receptivity coefficient is about three times smaller than for the smaller bluntness cases for this frequency. The most amplified frequency for the bluntness b = 0.01 is about F=0.30*10^{-5} and the receptivity coefficient will be even smaller than this due to the attenuation of the disturbances in the leading edge region.

Figures 15 and 16 show the results for the blunt wedge cases with a small bluntness r_0 = 0.001. The non-dimensional frequency and the spanwise wave number are F=1.25*10^{-5} and β = 0.025. Figure 15 shows the results for the evolution of the unsteady fluctuations obtained from the simulation for the slow wave at a fixed time. Figure 15(a) shows the contours of the density fluctuations in the entire domain and Fig. 15(b) depicts the results inside the boundary layer. It is seen that the region between the boundary

layer and the shock is quieter and the acoustic disturbances are not transmitted across the shock. This was also observed in Ref. 13 and 14 where the effect of acoustic incident angles on the generation and the evolution of disturbances over a blunt flat plate was investigated. It was found that the acoustic disturbances are weakly transmitted across the shock in the windward side and the receptivity coefficients are about two times higher in the leeward side than in the windward side. Figure 16 shows the amplitude of the pressure fluctuations along the wall in a log scale and Fig. 16 also includes the results from the parabolized stability equations (PSE) computations obtained for the same mean boundary layer profiles. The figures clearly show the initial generation and the eventual exponential growth of the instability waves inside the boundary layer. The computed receptivity coefficient is

$$C_{recpt,p_{wall},S} = 0.20$$

This is about six times smaller than that in the flat plate case with the same bluntness. However, if the acoustic disturbances are impinging at an angle, as was discussed previously, the receptivity coefficient may be larger than that for this case.

Discussion and Conclusions

The receptivity and the stability of supersonic boundary layers over a blunt flat plate and blunt wedge with 10 degrees wedge angle are numerically investigated at a free stream Mach number of 3.5 and at a Reynolds number of $1.0*10^6$/inch. Both the steady and unsteady solutions are obtained by solving compressible Navier-Stokes equations using the 5^{th}-order accurate weighted essentially non-oscillatory (WENO) scheme for space discretization and using a third-order total-variation-diminishing (TVD) Runge-Kutta scheme for time integration. Computations are performed for different leading edge bluntness b = 0.0001, 0.001, 0.005, 0.01 inches in the flat plate case and r_0 = 0.001 and 0.01 inches in the wedge case.

The results show that the bluntness has a strong stabilizing effect on the stability of the boundary layers. This stabilization is stronger in the flow over wedges than over flat plates. The transition Reynolds number increases slowly up to a nose Reynolds number of 1000 and increases sharply at higher nose Reynolds numbers. The transition Reynolds number for a flat plate with leading edge thickness of 0.01 inches is about 3.5 times larger than that for the Blasius boundary layer and it is about 7.2 times for the wedge. This is due to the entropy layers that are generated near the leading edges. These layers persist for longer distances with increasing bluntness. There may be other unstable modes in the entropy layer as were observed in the experiments[3] other than the first-mode type instabilities that were considered in this paper. Whether they exist and what role these waves play in the transition process still has to be investigated.

The receptivity coefficients for the flat plates are almost the same at small bluntness b = 0.0001 and 0.001 inches and they are much smaller in the higher bluntness case b = 0.01 inches. The receptivity coefficient for the wedge is six times smaller compared to the flat plate for the small bluntness case b = 0.001 inches. The receptivity coefficients at non-zero acoustic incident angles may be larger than is obtained at zero incident angles. These computations have to be carried out to find the largest receptivity coefficients in the wedge case.

References

1. P. Balakumar, "Transition in a Supersonic Boundary layer Due to Roughness and Acoustic Disturbances," *AIAA Paper 2003-3589*, 2003.
2. P. Balakumar, "Transition in a Supersonic Boundary layer Due to Acoustic Disturbances," *AIAA Paper 2005-0096*, 2005.

3. Stetson, K. F., Thompson, E. R., Donaldson, J. C., and Siler, L. G., "Laminar Boundary Layer Stability Experiments on a Cone at Mach 8, Part 2: Blunt Cone," AIAA 22nd Aerospace Sciences Meeting, Reno, Nevada, January 9-12, *AIAA Paper 84-0006*, 1984.
4. Reshotko, E. and Khan, M. M. S., " Stability of the Laminar Boundary Layer on a Blunted Plate in Supersonic Flow," *IUTAM Laminar-Turbulent Transition Symposium*, Stuttgart, F.R.G, September 1979.
5. Malik, M. R., Spall, R. E., and Chang, C. L., " Effect of Nose Bluntness on Boundary Layer Stability and Transition," *AIAA Paper 90-0112*, 1990.
6. Hu, S. E., and Zhnog, X., " Hypersonic Boundary-Layer Stability over Blunt Leading Edges with Bow-Shock Effects," *AIAA Paper 98-0433*, 1998.
7. Zhnog, X., and Ma, Y., " Receptivity and Linear Stability of Stetson's Mach 8 Blunt Cone Stability Experiments," *AIAA Paper 2002-2849*, 2002.
8. John, C. Evvard, "Transition studies on blunted bodies at supersonic speeds," *Presented at 9th International Congress of Applied Mechanics*, Brussels, Sept, 5-13, 1956.
9. Shu, Chi-Wang, " Essentially Non-Oscillatory and Weighted Essentially Non-Oscillatory Schemes for Hyperbolic Conservation Laws," *NASA/CR-97-206253 and ICASE Report* N0. 97-6
10. Atkins, H. L., "High-Order ENO Methods for the Unsteady Compressible Navier-Stokes Equations," *AIAA Paper 91-1557*, 1991.
11. Balakumar, P., Zhao, H., and Atkins, H., "Stability of Hypersonic Boundary_layers Over a Compression Corner," *AIAA Paper* 2002-2848, 2002.
12. Chen, F. J., Malik, M. R., Beckwith, I. E., "Comparison of Boundary Layer transition on a Cone and Flat Plate at Mach 3.5," *AIAA-88-0411*, 1988.
13. Egorov, I. V., Fedorov, A. V., and Soudakov, V. G., "Direct numerical simulation of supersonic boundary-layer receptivity to acoustic disturbances," *AIAA Paper* 2005-97, 2005.
14. M. R. Malik and P. Balakumar, "Receptivity of Supersonic Boundary Layers to Acoustic Disturbances," *AIAA Paper 2005-5027*, 2005.

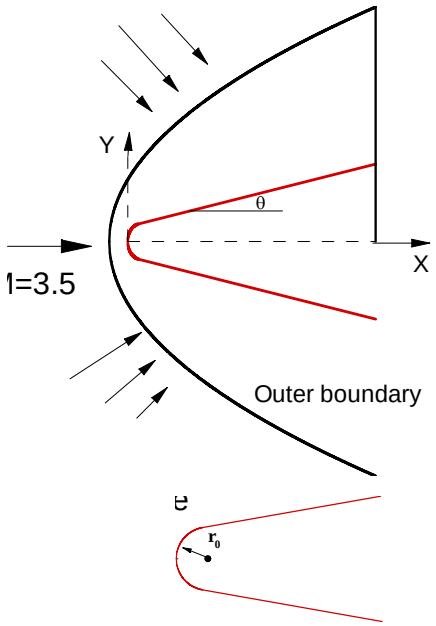

$M_\infty = 3.5$

Re $= 1.0*10^6$ /in., $4.0*10^6$/in.

$T_\infty = 156.42$ ° R

$T_{wall} = 476.0$° R

Leading edge radius $r_0 = 0.0001, 0.001, 0.01$ in.

Wedge half-angle = 0 and 10 degrees.

Figure 1. Schematic diagram of the computational model.

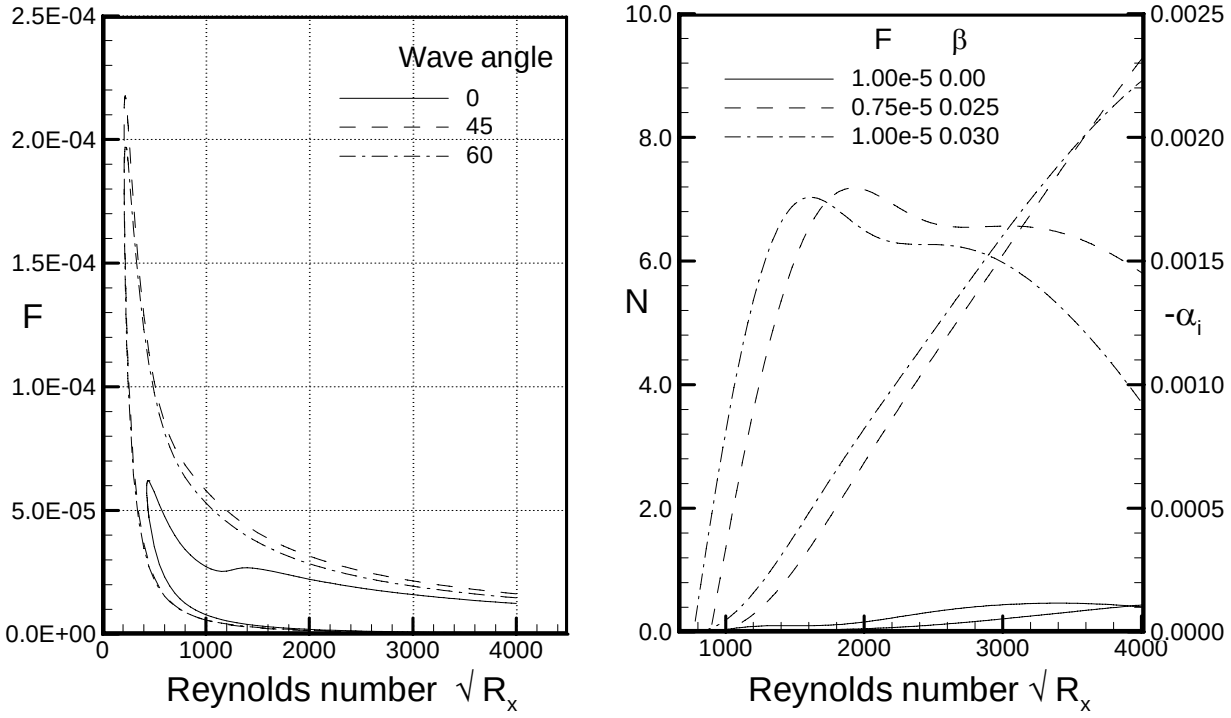

Figure 2. Stability and N-Factor diagrams for a similarity boundary layer. $M_\infty = 2.9$, $T_\infty = 200^\circ$.

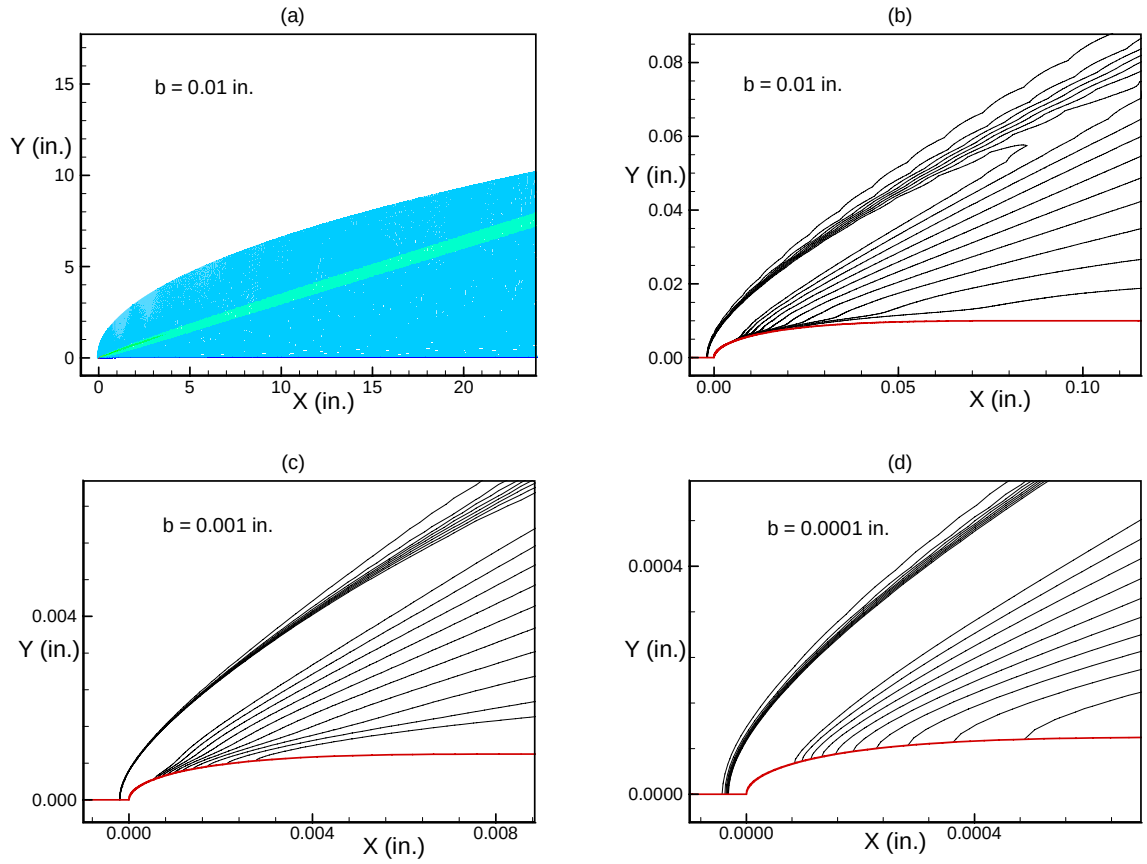

Figure 3. Contours of the density for flow over a flat plate with different bluntness at *M* = 3.5. (a) b = 0.01 in. (b) b = 0.01 in. (c) b = 0.001 in. (d) b = 0.0001 in.

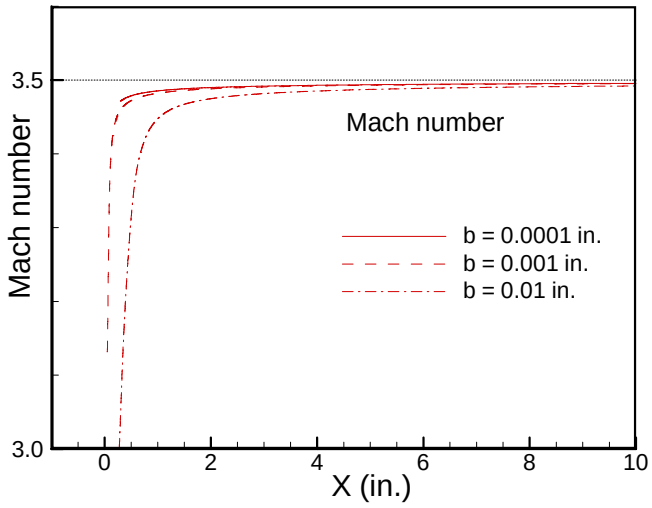

Figure 4. Mach number distribution at the edge of the boundary layer for different bluntness b = 0.0001, 0.001, 0.01 in. at *M* = 3.5.

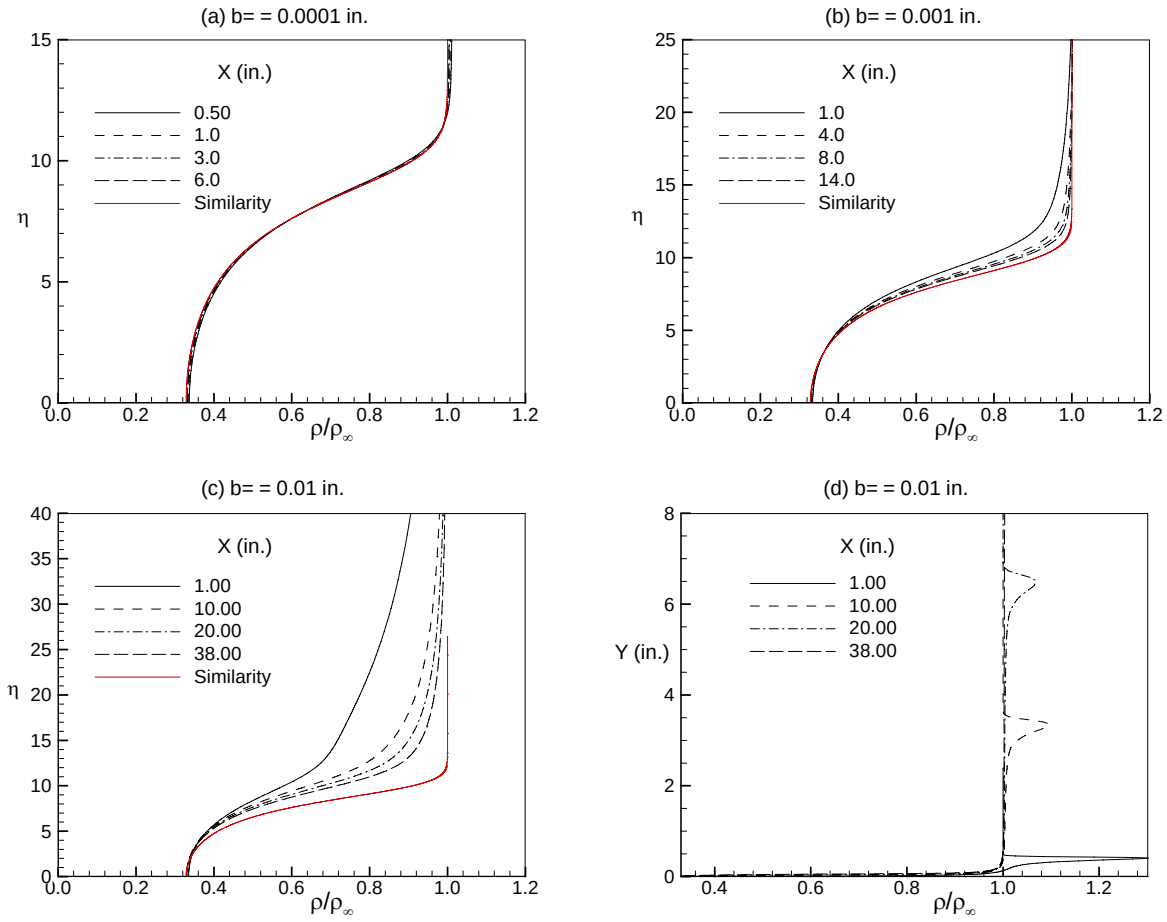

Figure 5. Density profiles at different X stations for b = 0.0001, 0.001, 0.01 in. at *M* = 3.5.

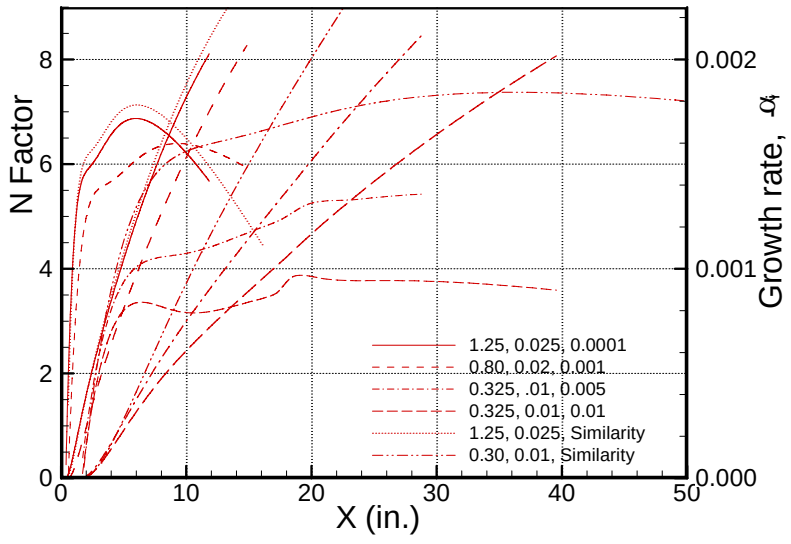

Figure 6. N-Factors and the growth rates for the most amplified disturbances b = 0.0001, 0.001, 0.01 in. at *M* = 3.5.

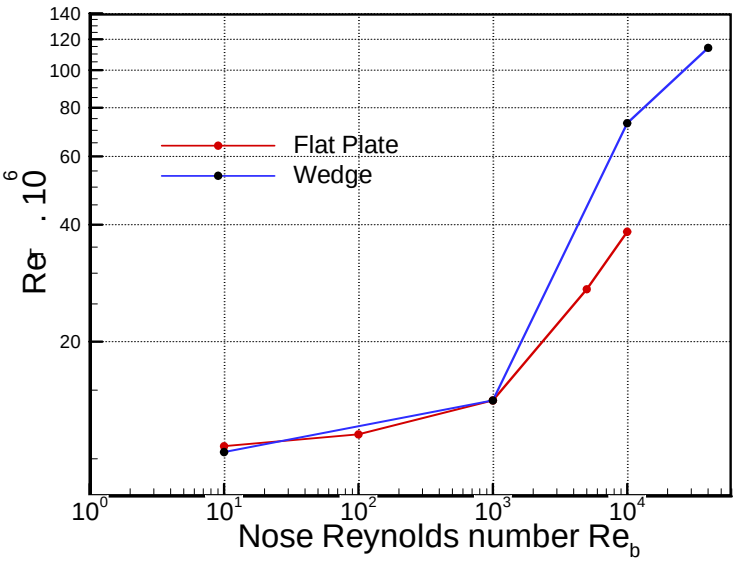

Figure 7. Transition Reynolds number for the flat plate and the wedge for different bluntness b = 0.0001, 0.001, 0.005, 0.01 in. at *M* = 3.5.

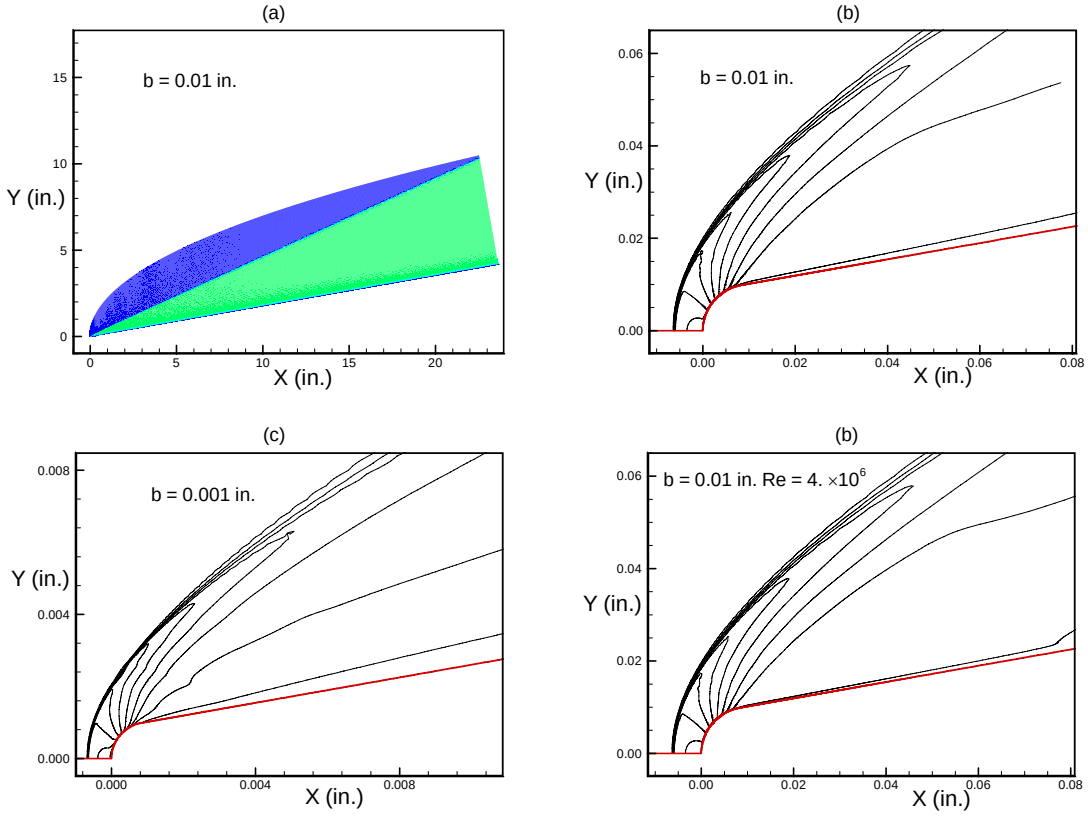

Figure 8. Contours of the density for flow over wedges with different bluntness at *M* = 3.5. Wedge angle is 10°. (a) r_0 = 0.001 in. Re=1.0*10^6/in. (b) r_0 = 0.01 in. Re=1.0*10^6/in. and (c) r_0 = 0.1 in. Re=4.0*10^6/in.

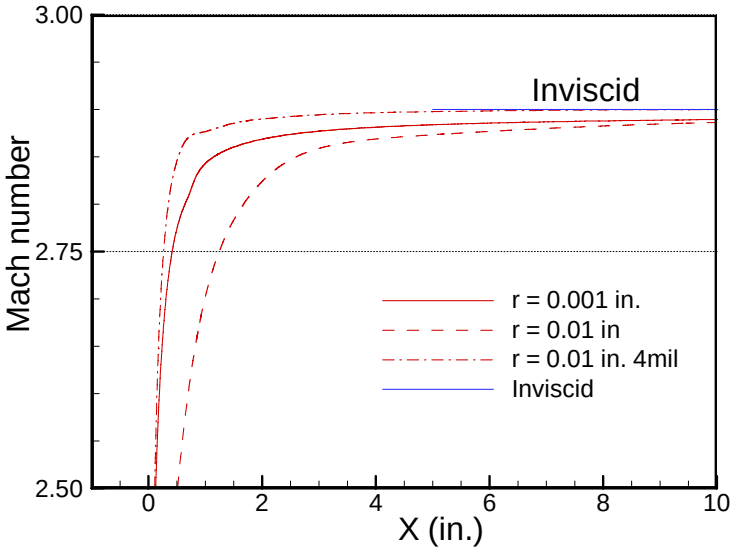

Figure 9. Mach number distribution along the surface for a wedge of 10 degrees for different bluntness r_0 = 0.001, 0.01, 0.01(Re=4.0*10^6/in.) in. at *M* = 3.5.

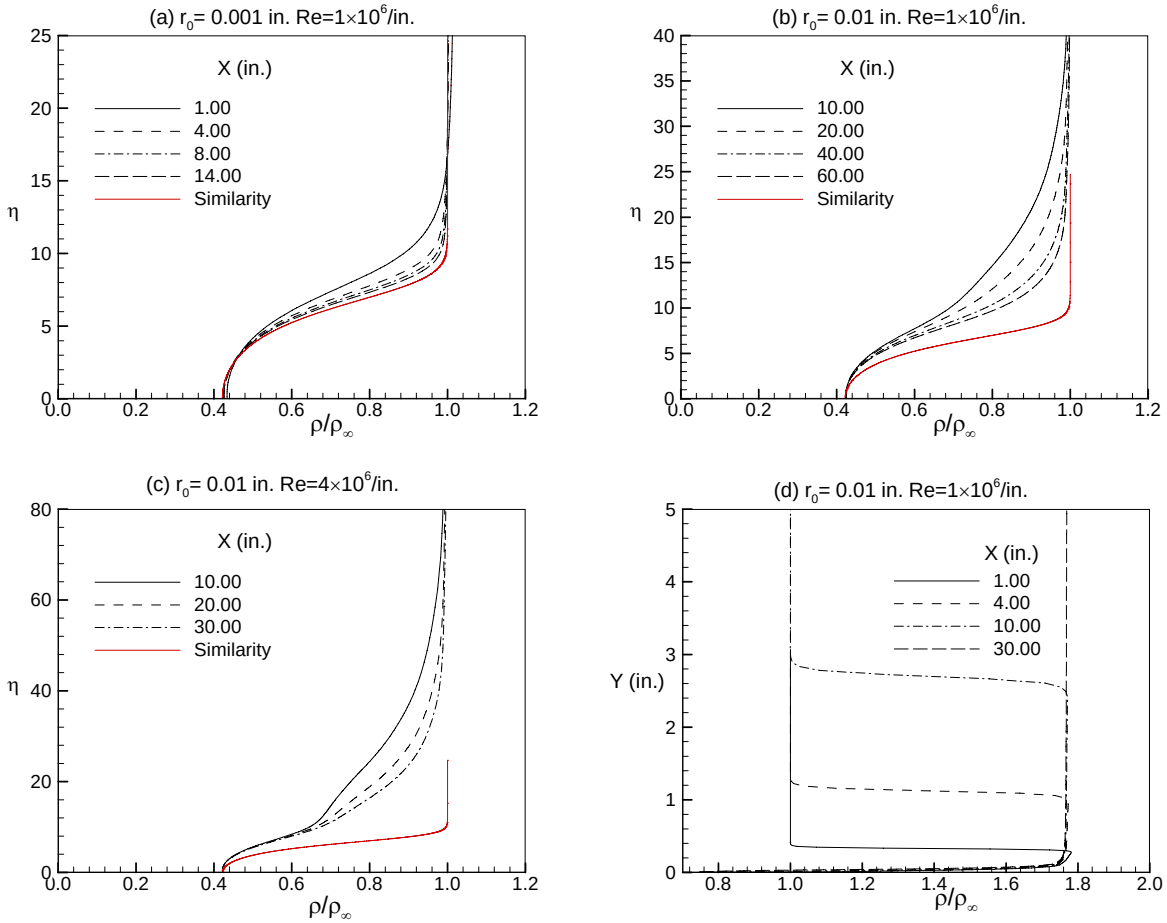

Figure 10. Density profiles at different X stations for r_0 = 0.001, 0.01, 0.01 in. at *M* = 3.5.

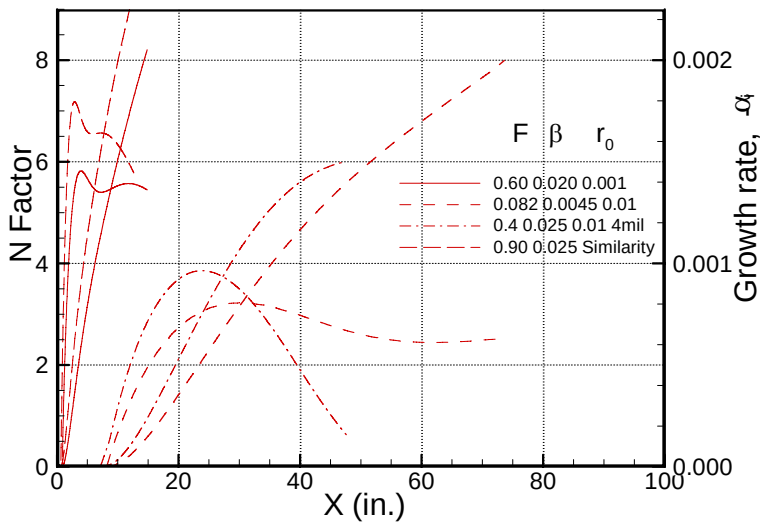

Figure 11. N-Factors and the growth rates for the most amplified disturbances for r_0 = 0.001, 0.01, 0.01 in. at *M* = 3.5.

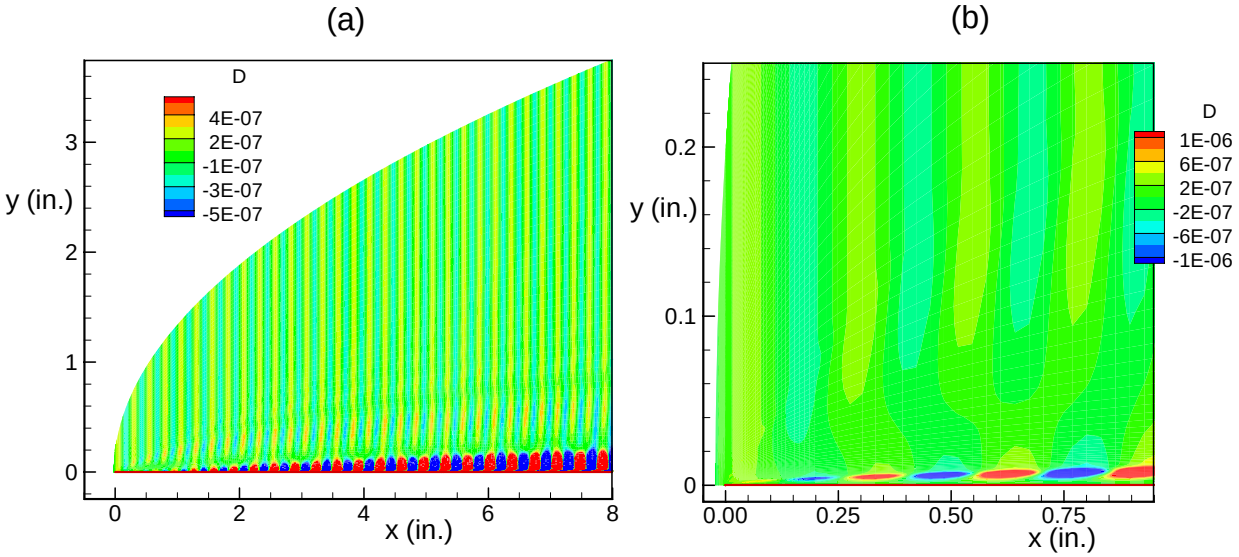

Figure 12. Contours of the unsteady density fluctuations due to the interaction of a 3D slow acoustic wave with a blunt flat plate b = 0.0001 inch. *F* = 1.25*10^{-4}, *β* = 0.025, incident angle 0.0.

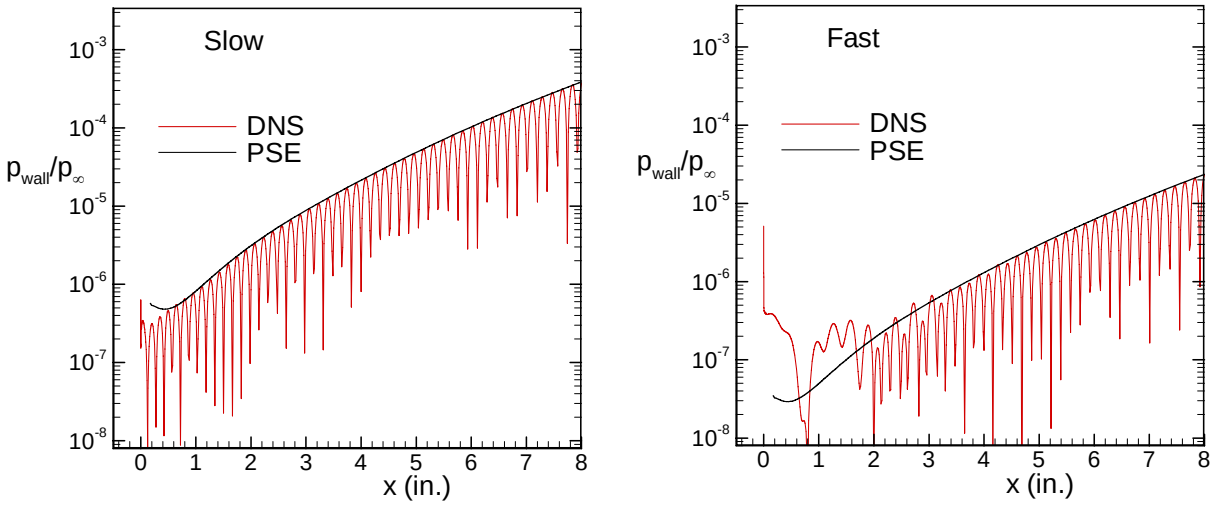

Figure 13. Amplitude of the pressure fluctuation at the wall and comparison with the PSE. F=1.25*10^{-4}, β = 0.025, b = 0.0001 inch.

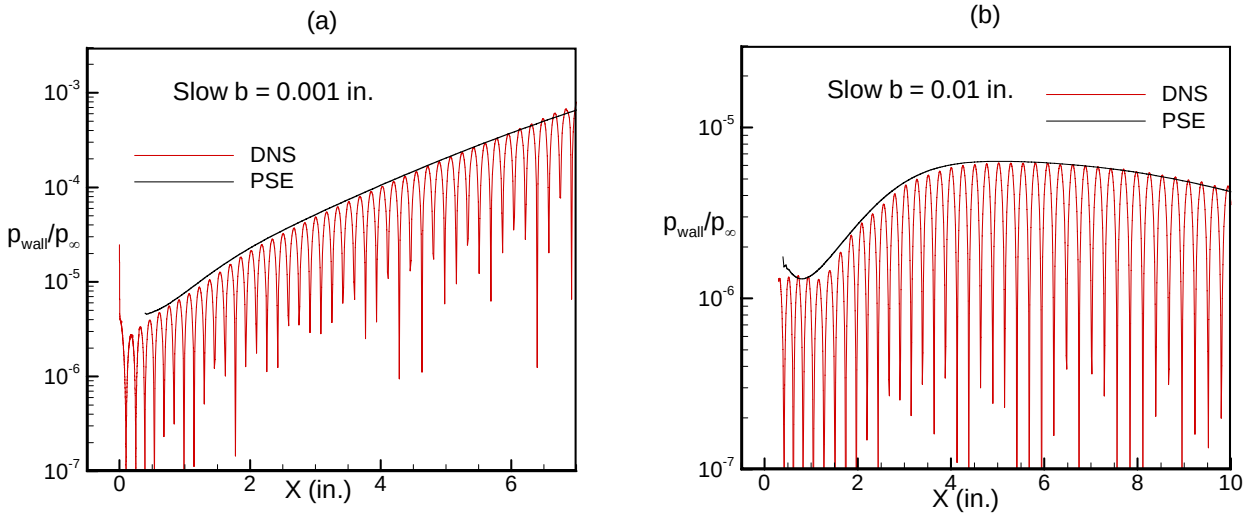

Figure 14. Amplitude of the pressure fluctuation at the wall and comparison with the PSE. (a) F=1.25*10^{-4}, β = 0.025 , b = 0.001 in. (b) F=0.75*10^{-4}, β = 0.025 , b = 0.01 in.

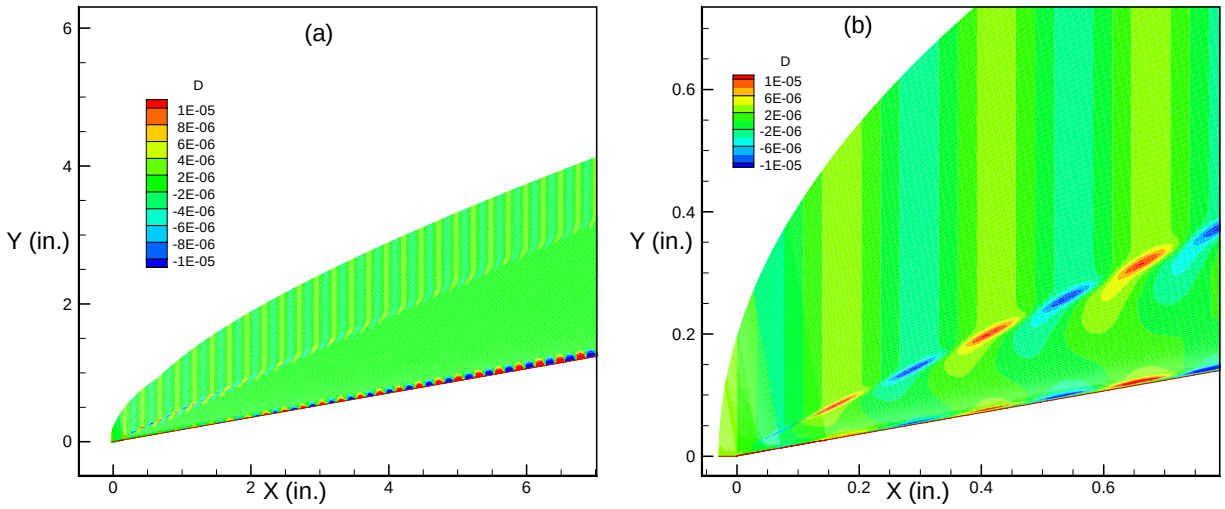

Figure 15. Contours of the unsteady density fluctuations due to the interaction of a 3D slow acoustic wave with a blunt wedge r_0 = 0.001 inches. F = 1.25*10^{-4}, β = 0.025, incident angle 0.0.

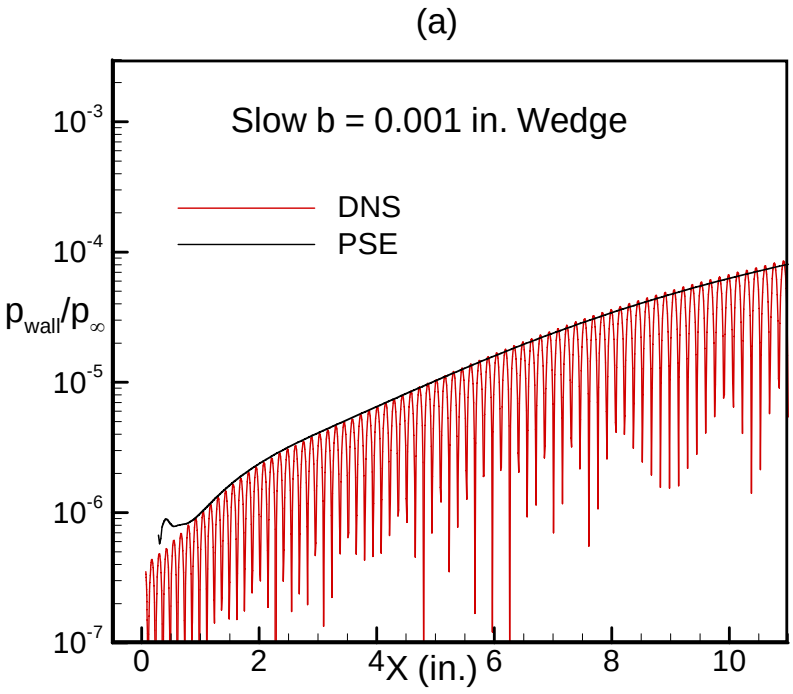

Figure 16. Amplitude of the pressure fluctuation at the wall and comparison with the PSE. F=1.25*10^{-4}, β = 0.025.